Acta Neuropathologica (2023) 145:325–333
https://doi.org/10.1007/s00401-022-02533-1

ORIGINAL PAPER

Cryo-EM structures of amyloid-β filaments with the Arctic mutation (E22G) from human and mouse brains

Yang Yang[1] · Wenjuan Zhang[1,6] · Alexey G. Murzin[1] · Manuel Schweighauser[1] · Melissa Huang[1,7] · Sofia Lövestam[1] · Sew Y. Peak-Chew[1] · Takashi Saito[2,8] · Takaomi C. Saido[2] · Jennifer Macdonald[1] · Isabelle Lavenir[1] · Bernardino Ghetti[3] · Caroline Graff[4,5] · Amit Kumar[4] · Agneta Nordberg[4,5] · Michel Goedert[1] · Sjors H. W. Scheres[1]

Received: 2 November 2022 / Revised: 15 December 2022 / Accepted: 15 December 2022 / Published online: 7 January 2023

Abstract

The Arctic mutation, encoding E693G in the *amyloid precursor protein (APP)* gene [E22G in amyloid-β (Aβ)], causes dominantly inherited Alzheimer's disease. Here, we report the high-resolution cryo-EM structures of Aβ filaments from the frontal cortex of a previously described case (*AβPParc1*) with the Arctic mutation. Most filaments consist of two pairs of non-identical protofilaments that comprise residues V12–V40 (human Arctic fold A) and E11–G37 (human Arctic fold B). They have a substructure (residues F20–G37) in common with the folds of type I and type II Aβ42. When compared to the structures of wild-type Aβ42 filaments, there are subtle conformational changes in the human Arctic folds, because of the lack of a side chain at G22, which may strengthen hydrogen bonding between mutant Aβ molecules and promote filament formation. A minority of Aβ42 filaments of type II was also present, as were tau paired helical filaments. In addition, we report the cryo-EM structures of Aβ filaments with the Arctic mutation from mouse knock-in line App^{NL-G-F}. Most filaments are made of two identical mutant protofilaments that extend from D1 to G37 (App^{NL-G-F} murine Arctic fold). In a minority of filaments, two dimeric folds pack against each other in an anti-parallel fashion. The App^{NL-G-F} murine Arctic fold differs from the human Arctic folds, but shares some substructure.

Keywords Alzheimer's disease · Amyloid-beta · Arctic mutation · Electron cryo-microscopy · Mouse App^{NL-G-F} knock-in line · Tau

Introduction

Dominantly inherited mutations in the amyloid precursor protein gene (*APP*) that cause disease are a mainstay of the amyloid cascade hypothesis of Alzheimer's disease (AD) [11, 14]. They have shown that overexpression of wild-type amyloid-β peptide (Aβ) or an increase in the ratio of Aβ peptides of 42–40 residues (Aβ42/Aβ40) is sufficient to cause familial AD. We recently reported that Aβ42 filaments from sporadic and inherited (APP_{V717F} and $PSEN1_{F105L}$) cases of AD share identical structures [37]. These mutations lead to the deposition of wild-type Aβ42.

✉ Michel Goedert
mg@mrc-lmb.cam.ac.uk

✉ Sjors H. W. Scheres
scheres@mrc-lmb.cam.ac.uk

1 Medical Research Council Laboratory of Molecular Biology, Cambridge, UK

2 RIKEN Brain Science Institute, Saitama, Japan

3 Department of Pathology and Laboratory Medicine, Indiana University School of Medicine, Indianapolis, IN, USA

4 Department of Neurobiology, Care Sciences and Society, Karolinska Institutet, Stockholm, Sweden

5 Theme Inflammation and Aging, Karolinska University Hospital, Stockholm, Sweden

6 Present Address: Medical Research Council Prion Unit and Institute of Prion Diseases, University College London, London, UK

7 Present Address: Dementia Research Institute, Department of Clinical Neurosciences, University of Cambridge, Cambridge, UK

8 Present Address: Department of Neurocognitive Science, Nagoya City University, Nagoya, Japan

Several mutations in *APP* give rise to mutant Aβ, including dominantly inherited APP_{E693G} (Arctic mutation) [17, 25], APP_{E693K} (Italian mutation) [5] and APP_{E693Q} (Dutch mutation) [22], as well as recessively inherited $APP_{\Delta E693}$ (Osaka mutation) [35]. The structures of mutant Aβ filaments from brain are not known. Mutations E693K and E693Q give rise to cerebral amyloid angiopathy, resulting in focal symptoms related to recurrent strokes [3, 5]. Many mutation carriers also develop dementia, which often follows the strokes. Aβ deposits are more abundant in cerebral blood vessels than in brain parenchyma and there are no abundant neuritic plaques or tau inclusions.

In contrast, mutations E693G and ΔE693 cause early-onset AD. For the Arctic mutation, unlike in sporadic AD, symptomatic carriers are negative for Pittsburgh compound B (PiB) by positron emission tomography (PET) [30]. Like in sporadic AD, they show reduced Aβ42 and elevated total tau and P-tau in cerebrospinal fluid, as well as cerebral hypometabolism, measured by ^{18}F-fluorodeoxyglucose PET [21, 26, 34]. By immunohistochemistry, amyloid plaques appear to be ring-shaped, contain truncated Aβ40 and Aβ42, and lack a congophilic core [1, 16]. A ring shape is observed predominantly with Aβ42 antibodies, with Aβ40 staining being distributed more homogenously through plaques [21].

The Arctic mutation causes diminished rather than increased levels of Aβ40 and Aβ42 in conditioned media from transfected cells [32]. This paradox has been explained by the finding that E22G Aβ40 forms what has been described as protofibrils at a faster rate and in larger number than wild-type Aβ40 [25]. Increased assembly of Aβ with the Arctic mutation compared to wild-type was greater for Aβ40 than for Aβ42 [23]. Based on the results with the Arctic mutation and other findings, it has been proposed that the neurotoxic effects of Aβ are mainly mediated by oligomers and protofibrils rather than filaments [4, 19, 36]. In cases of AD with the Arctic mutation, tau pathology was mainly in the form of neuropil threads, but neurofibrillary tangles and neuritic plaques were also present [16].

To improve our understanding of the molecular mechanisms of disease, experimental model systems that reflect what happens in the human brain are needed. Mouse knock-in lines App^{NL-F} and App^{NL-G-F} develop abundant deposits of humanized Aβ, in the absence of overexpression of APP [28]. They use (numbering of human APP) the Swedish (KM670/671NL) and Beyreuther/Iberian (I716F) mutations. The Swedish double mutation elevates the total amount of Aβ40 and Aβ42, whereas the Beyreuther/Iberian mutation increases the ratio of Aβ42 to Aβ40. App^{NL-F} mice deposit wild-type human Aβ, whereas App^{NL-G-F} mice deposit human Aβ with the Arctic mutation (E22G). We showed previously that Aβ filaments extracted from the brains of App^{NL-F} mice are identical to type II Aβ42 filaments from human brains [37].

Here, we show that the structures of mutant Aβ filaments from the frontal cortex of an individual with missense mutation E693G in *APP* differ from those of wild-type Aβ filaments. We also show that the structures of Aβ filaments from homozygous mice of knock-in line App^{NL-G-F} differ from those present in human brains.

Materials and methods

Genetics and clinical history

We determined the cryo-EM structures of Aβ and tau filaments from the frontal cortex of a previously described female individual (*AβPParc1*) with mutation E693G in APP [21, 30]. The presence of a heterozygous *APP* Arctic mutation (c.2078A > G) in exon 17 was confirmed by re-sequencing of DNA extracted from the blood of the tissue donor. AmpliTaqGold 360 PCR Master Mix (Thermo Fisher Scientific) was used for PCR amplification. Primer sequences and PCR conditions are available upon request. Sanger sequencing in both directions was performed using the BigDye Terminator v3.1 cycle sequencing kit (Thermo Fisher Scientific) and analyzed using an ABI3500 genetic analyzer. As reported [30], the proband began to experience cognitive symptoms at the age of 53 years, was diagnosed with AD at age 62 and died aged 66. The neuropathological characteristics of case *AβPParc1* have been described [30].

App^{NL-G-F} knock-in mice

We determined the cryo-EM structures of Aβ filaments from the brain of a 22-month-old homozygous App^{NL-G-F} knock-in mouse on a C57 BL/6 JAX background. Beginning at 2 months of age, these mice form abundant extracellular deposits that are made of human Aβ with Arctic mutation E22G [28]. They carry the Swedish double mutation (KM670/671NL), the Arctic mutation (E693G) [E22G in humanized Aβ] and the Beyreuther/Iberian mutation (I716F) in APP.

Extraction of filaments

For cryo-EM analysis of the human sample, sarkosyl-insoluble material was extracted from temporal cortex of case *AβAPParc1,* essentially as described [33]. Briefly, tissues were homogenized in 20 vol (w/v) extraction buffer consisting of 10 mM Tris–HCl, pH 7.4, 0.8 M NaCl, 10–20% sucrose and 1 mM EGTA. Homogenates were brought to 2% sarkosyl and incubated for 60 min at 37 °C. Following a 10 min centrifugation at 10,000*g*, the supernatants were spun at 100,000*g* for 60 min. The final pellets were resuspended in 100 µl/g of 20 mM Tris–HCl, pH 7.4, 50 mM

NaCl. For cryo-EM analysis of the mouse samples, sarkosyl-insoluble material was extracted from whole brains of mouse knock-in line App^{NL-G-F}. Tissues were homogenized in 20 vol (w/v) extraction buffer consisting of 20 mM Tris–HCl, pH 7.4, 0.8 M NaCl, 15% sucrose, 5 mM EGTA, 1% sarkosyl and protease inhibitor (1 tablet per 10 ml, Roche), and incubated for 60 min at room temperature. Following a 20 min centrifugation at 10,000*g*, the supernatants were spun at 124,000*g* for 45 min at 20 °C. The pellets were resuspended in 200 µl extraction buffer, followed by a second spin at 124,000*g*. Pellets were then resuspended as above, followed by a third spin at 124,000*g*. The final pellets were resuspended in 33–100 µl/g of 20 mM Tris–HCl, pH 7.4, 200 mM NaCl and used for cryo-EM analysis.

Mass spectrometry

Mass spectrometry was performed as described [24]. Sarkosyl-insoluble pellets were resuspended in 1 ml/g extraction buffer and centrifuged at 3000*g* for 5 min. The supernatants were diluted threefold in 50 mM Tris–HCl, pH 7.4, containing 0.15 M NaCl, 10% sucrose and 0.2% sarkosyl, and spun at 100,000*g* for 60 min. The pellets were resuspended in 100 µl hexafluoroisopropanol. Following a 3 min sonication at 50% amplitude (QSonica), they were incubated at 37 °C for 2 h and centrifuged at 100,000*g* for 15 min, before being dried by vacuum centrifugation. Matrix-assisted laser desorption/ionization time of flight (MALDI-TOF) mass spectrometry was carried out as described [37].

Electron cryo-microscopy

For cryo-EM, extracted Aβ filaments were centrifuged at 3000*g* for 2 min and treated with 0.4 mg/ml pronase for 30–60 min [12]. Holey carbon grids (Quantifoil AuR1.2/1.3, 300 mesh) were glow-discharged with an Edwards (S150B) sputter coater at 30 mA for 30 s. Three µl aliquots were applied to the grids and blotted for 3–5 s with filter paper at 100% humidity and 4 °C using a Thermo Fisher Vitrobot Mark IV. Datasets were acquired on Thermo Fisher G2 and G3 microscopes, with Gatan K3 detectors in counting mode, using a Bioquantum energy filter (Gatan) with a slit width of 20 $e^{-}V$. Images were recorded with a total dose of 40 electrons per $Å^2$.

Helical reconstruction

All super-resolution frames were gain-corrected, binned by a factor of 2, aligned, dose-weighted and then summed into a single micrograph using RELION's own implementation of MotionCor2 [39]. Contrast transfer function (CTF) parameters were estimated using CTFFIND-4.1 [27]. Subsequent image-processing steps were performed using helical reconstruction methods in RELION [15, 40]. Filaments were picked manually [dataset from frontal cortex of human Arctic case] or automatically using Topaz in RELION [dataset from brains of App^{NL-G-F} knock-in mice] [2]. Reference-free 2D classification was performed to identify homogeneous segments for further processing. Initial 3D reference models were reconstructed de novo from 2D class averages [29] using an estimated rise of 4.75 Å and helical twists according to the observed cross-over distances of filaments in the micrographs. To increase the resolution of the reconstructions, Bayesian polishing and CTF refinement were performed [41]. Final 3D reconstructions, after auto-refinement, were sharpened using the standard post-processing procedures in RELION, and resolutions calculated from Fourier shell correlations at 0.143 between the two independently refined half-maps, using phase-randomization to correct for convolution effects of a generous, soft-edged solvent mask. Further details of data acquisition and processing are given in Table S1.

Model building and refinement

Atomic models were built manually in Coot [7]. Coordinate refinements were performed using *Servalcat* [38]. Final models were obtained using refinement of only the asymmetric unit against the half-maps in *Servalcat*.

Results

Structures of Aβ filaments from case *AβPParc1*

We determined the cryo-EM structures of Aβ filaments from a case with mutation E693G in *APP* [E22G in Aβ] (Fig. 1a). Most filaments, solved to 2.0 Å resolution, are made of four mutant protofilaments, with two copies each of non-identical protofilaments A and B (Fig. 1b). The ordered cores of protofilaments A and B, hereafter referred to as the human Arctic folds A and B, consist of residues V12–V40 and E11–G37, respectively. Each fold comprises four β-strands (β1–β4) that extend from residues 12 to 15, 18 to 21, 30 to 32 and 34 to 36 in fold A, and from residues 11 to 13, 14 to 19, 30 to 32 and 34 to 36 in fold B (Fig. 1c). Human Arctic fold A is almost identical to the fold of type II protofilaments of wild-type Aβ42, but it is shorter by two C-terminal amino acids (Fig. 1d). Human Arctic fold B is three amino acids shorter at its C-terminus than fold A, with residues F20–G37 adopting an almost identical conformation to that of fold A. Segment E11–F19 of fold B is one amino acid longer than that of fold A and adopts a different conformation.

The substructures that are common to folds A and B form a dimeric and pseudo-symmetric interface that is centered on residues G25 and S26 from both folds and is stabilized

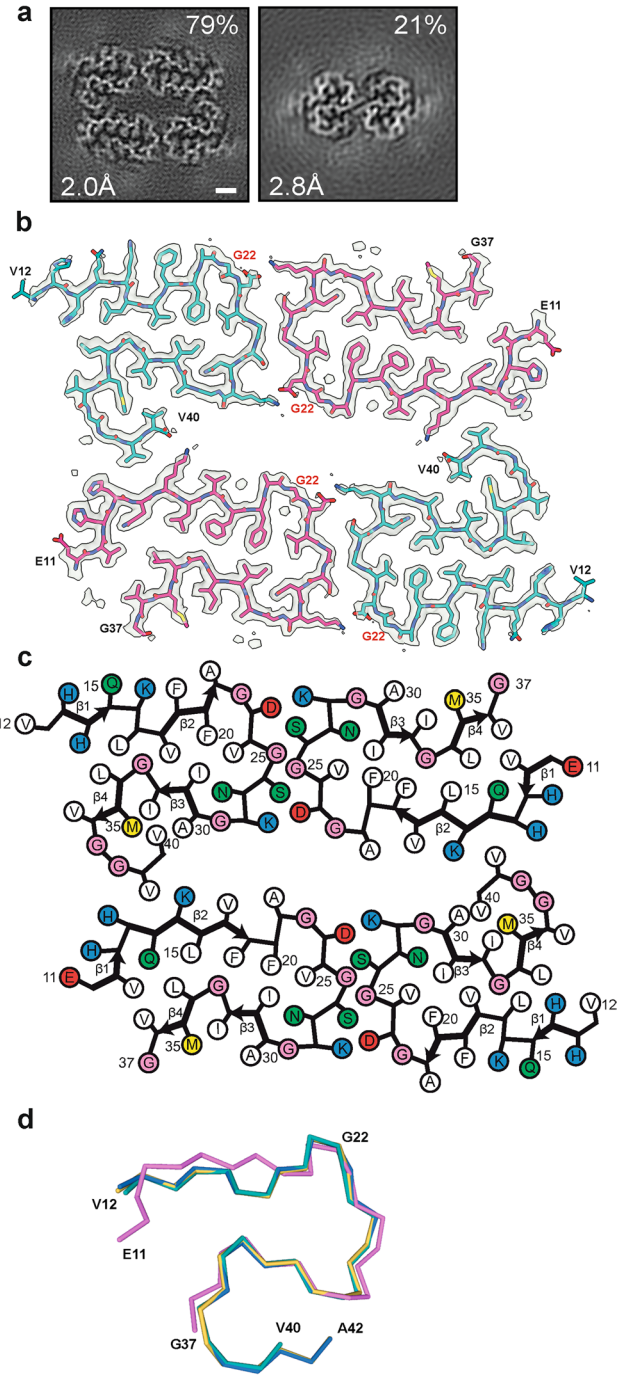

Fig. 1 The human Arctic folds of Aβ. **a** Cross sections of Aβ filaments from the frontal cortex of case *AβPParc1* perpendicular to the helical axis, with a projected thickness of approximately one rung. Percentages of filaments (relative to the total, taken as 100%) are shown on the top right. The resolutions of the cryo-EM maps are given on the bottom left (2.0 and 2.8 Å). Scale bar, 1 nm. **b** Cryo-EM density maps (in transparent gray) and atomic models of the human Arctic folds. Human Arctic fold A (cyan) and human Arctic fold B (magenta). **c** Schematic of human Aβ filaments with the Arctic mutation. Negatively charged residues are shown in red, positively charged residues in blue, polar residues in green, non-polar residues in white, sulfur-containing residues in yellow and glycines in pink. Thick connecting lines with arrowheads indicate β-strands. **d** Superposition of the backbone structures of human Arctic fold A (cyan), human Arctic fold B (magenta), human Arctic type II Aβ42 protofilament (yellow) and human wild-type type II Aβ42 protofilament (blue). The all-atom r.m.s.d. values for human Arctic fold A with human Arctic fold B (residues F20–G37), human Arctic type II Aβ42 (residues V12–V40) and human wild-type type II Aβ42 structures (residues V12–V40) were 2.2 Å, 0.3 Å and 0.3 Å, respectively

by salt bridges between D23 from one fold and K28 from the other fold, and vice versa. These doublets of protofilaments A and B pack together with C2 symmetry to form the tetrameric filaments. The interface between doublets is also stabilized by two salt bridges, between the main chain carboxyl group of the C-terminal residue V40 from protofilament A in one doublet and the side chain of K16 from protofilament B in the other doublet, and vice versa (Fig. 1b).

Besides tetrameric Aβ filaments, a minority of dimeric type II Aβ42 filaments was also present (Fig. 1a). Solved to 2.8 Å resolution, their structures suggest that they are made of mutant protein, but the presence of some wild-type Aβ42 cannot be excluded. Mass spectrometry of sarkosyl-insoluble fractions showed abundant mutant Aβ40 that was sequentially truncated at the N-terminus, and a smaller amount of wild-type Aβ42 (Fig. S1a). There was also a substantial amount of mutant Aβ species truncated at E3 or E11, with the glutamate residues having been converted to pyroglutamates.

The Arctic mutation lies in the substructure that is shared by wild-type and mutant Aβ folds. Our high-resolution cryo-EM maps of Aβ filaments with the Arctic mutation showed the absence of side chain densities at G22, unlike the corresponding maps for wild-type Aβ filaments (Fig. 2a–c). In filaments made of wild-type Aβ, the presence of a side chain at E22 restricts the orientation of the flanking main chain peptide groups and prevents the formation of hydrogen bonds linking these groups to those in other Aβ molecules. Removal of the side chains by the E22G mutation results in a slight reorientation of peptide groups in the "frustrated" loop F20–V24, which leads to increased hydrogen bonding between adjacent Aβ molecules (Fig. 2d, e).

Structures of tau filaments from case *AβPParc1*

Tau filaments were found in the sarkosyl-insoluble fractions from frontal cortex of case *AβPParc1*. Their cryo-EM structures were determined to a resolution of 2.9 Å and found to be identical to those of PHFs from AD and some other diseases (Fig. 3) [31]. Straight tau filaments were not observed.

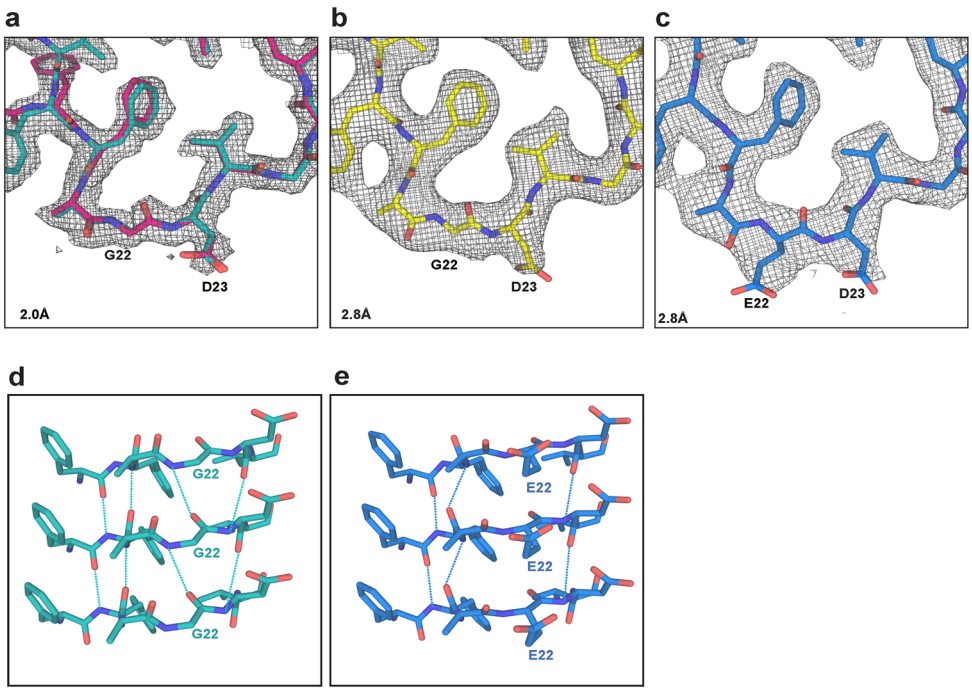

Fig. 2 Structures of the E22G site in human Arctic and type II Aβ42 filaments. **a** Structure of the F20–V24 arc of human Arctic fold A (cyan) superimposed on that of human Arctic fold B (magenta), and overlaid on the corresponding section of the 2.0 Å electron density map (gray). **b** Structure of the F20–V24 arc of E22G type II Aβ42 fold (yellow) overlaid on the corresponding section of the 2.8 Å electron density map (gray). **c** Structure of the F20–V24 arc of wild-type type II Aβ42 fold (blue) overlaid on the corresponding section of the 2.8 Å electron density map (gray). **d** Side view of structure of human Arctic fold A G22 (cyan), showing the presence of hydrogen bonds (dashed lines) between the main chain groups. **e** Side view of structure of human wild-type type II Aβ42 fold A E22 (blue), showing the presence of hydrogen bonds (dashed lines) between the main chain groups

Arctic fold of Aβ from *App*$^{NL-G-F}$ mouse brains

We also determined the cryo-EM structure of Aβ filaments from the brains of *App*$^{NL-G-F}$ mice to 3.5 Å resolution (Fig. 4). Filaments are made of two identical S-shaped mutant protofilaments that extend from D1 to G37 of Aβ (Fig. 4a, b). Each protofilament consists of five β-strands that extend from residues 1 to 8, 10 to 16, 17 to 19, 30 to 32 and 34 to 36 (Fig. 4c). Additional densities around K16 may be co-factors or post-translational modifications of mutant Aβ, but their chemical identity remains unknown. We name the conformation of these protofilaments the *App*$^{NL-G-F}$ murine Arctic fold.

It shares the substructure F20–G37 with human Arctic folds A and B, in which the backbone conformation of the loop F20–V24 differs from human Arctic folds in that the orientation of the peptide group between A21 and G22 is reversed. Flipping the peptide group does not affect its ability to form additional hydrogen bonds with other Aβ molecules, but places G22 in the glycine-only quadrant of the Ramachandran plot. The N-terminal segment (residues D1–F19) is longer than in human Arctic folds A and B, allowing it to fold back on the common substructure and extend across the dimeric interface towards the other protofilament (Fig. 4d). Both protofilaments pack against each other with pseudo-2_1 symmetry. The central portion of their interface is made of residues D23, G25 and S26 from both protofilaments and resembles the doublet-forming interface of human Arctic protofilaments A and B. At the edges, both protofilaments pack against each other through the hydrophobic side chains of A2 and F4 from one protofilament and A30, I32 and M35 from the other.

In addition, there are salt bridges between E11 and K28, and close contacts of the side chains of H6 and S8 with the backbone atoms of G29 and K28, respectively. We also observed a minority of wider filaments, in which two dimeric folds pack against each other in an anti-parallel fashion (Fig. 4a). From the cryo-EM maps, we only observed residues ranging from D1 to G37 of mutant Aβ, consistent with mass spectrometry, which indicated that most Aβ in the sample is mutant Aβ1–38 (Fig. S1b). It will be interesting to stain *App*$^{NL-G-F}$ brains from old mice with antibodies specific for C-terminally truncated Aβ.

Discussion

We report the first structures of filaments made of human mutant Aβ from brain. Tetrameric filaments containing the E22G Arctic mutation differ from dimeric type I and type II filaments of wild-type Aβ42. However, there is a large common substructure that is shared between protofilaments. Comparison of local conformations in this region revealed the presence of additional hydrogen bonds between adjacent Aβ molecules in mutant protofilaments; these hydrogen bonds cannot form in wild-type protofilaments, providing a plausible explanation for the increased fibrillogenesis of E22G Aβ. Mutation E22G may have an

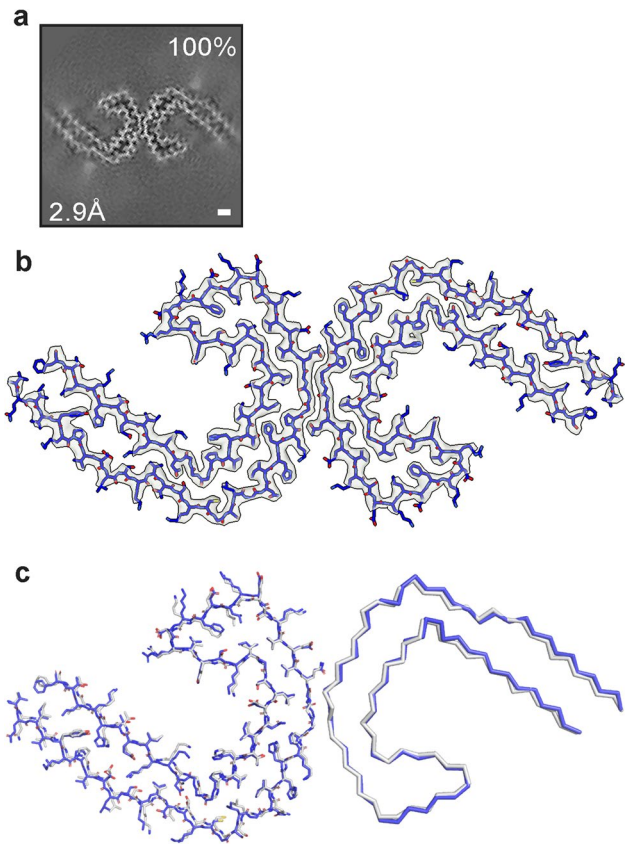

Fig. 3 PHF tau filaments from case *AβPParc1*. **a** Cross sections of tau filaments from the frontal cortex perpendicular to the helical axis, with a projected thickness of approximately one rung. Percentage of filaments (relative to the total taken as 100%) are shown on the top right. The estimated resolution of the cryo-EM map is given on the bottom left (2.9 Å). **b** Cryo-EM density map (gray) and atomic model of PHF (blue) from a human case with the Arctic mutation. **c** Comparison of the PHF structure from case *AβPParc1* (blue) with the PHF structure from sporadic Alzheimer's disease brain (gray) (PDB 5O3L). The structures are shown as sticks for one protofilament and as ribbons for the other protofilament

additional fibrillation-promoting effect, which is the relief of electrostatic repulsion as a result of removal of the negatively charged carboxylic group of E22; in the wild-type structure, E22 is trapped in close proximity to the carboxylic group of D23 [37]. Dutch (E693Q) and Italian (E693K) mutations in *APP* may have a similar electrostatic effect, provided they form filaments with the same common substructure at the mutation site.

Mass spectrometry of sarkosyl-insoluble material indicates the presence of an N-terminal fuzzy coat of Aβ and shows that most mutant peptides end at residue V40. Similar mass spectrometry results have been reported from temporal cortex of another individual with the Arctic mutation [26]. In agreement with these observations, immunohistochemistry of cerebral cortex from case *AβPParc1* has shown stronger staining for Aβ40 than for Aβ42 [21]. These observations agree with our structures. In the majority of filaments, half of the protofilaments (human Arctic fold A) are made of Aβ40, with the terminal carboxyl group of V40 contributing to the protofilament interface, whereas the other half (human Arctic fold B) may contain a variable number of residues after G37. Only a minority of filaments is made of mutant Aβ42. Apart from a lack of side chain density at G22, their structure is identical to type II Aβ42 filaments made of wild-type protein [37]. In these dimeric filaments, the terminal carboxyl group of A42 contributes to the protofilament interface. These findings establish that the parenchymal deposits of E22G Aβ differ from those of wild-type Aβ by the presence of abundant Aβ40 filaments. In sporadic AD, wild-type Aβ42 predominates in parenchymal plaques and wild-type Aβ40 in blood vessel deposits [18, 37]. The mechanisms underlying these differences remain to be identified.

Co-deposition of wild-type Aβ and E22G Aβ has been described [26], suggesting a link between their assemblies. Our findings further suggest that wild-type and mutant Aβ may co-assemble in individual filaments. Incorporation of a small amount of wild-type Aβ in filaments made of E22G Aβ would not result in steric clashes and would probably not be visible in the cryo-EM density maps.

A model of human mutant Aβ40 filaments made of two copies of Arctic fold A displays an intriguing similarity with the structures of wild-type Aβ40 filaments from the meninges of AD brains (Fig. S3) [18]. This model of the Arctic fold A dimer fits into the 4.4 Å resolution density map of dimeric Aβ40 from the meninges of AD brains, the original chain trace of which differs from our model by the presence of the complete N-terminus and swapping of the C-terminal segments of two protofilaments at G25, the point where the protofilament backbones are the closest to each other. A more detailed comparison awaits a higher resolution structure of Aβ40 filaments from meninges, but this similarity hints at the possibility of filament formation in blood vessels being seeded by the substructures shared with Aβ filaments from brain parenchyma.

The large common substructures shared by human Arctic folds and wild-type Aβ42 filaments contain β-strands, like other amyloids. Thus, PiB-PET negativity of APP_{E693G} cases [30] does not reflect the absence of amyloid; it suggests instead that PiB does not recognize the fold of E22G Aβ. The same may be true of the Osaka mutation [35]. It remains to be determined how these structures relate to what has been referred to as 'protofibrils' based on assembly experiments of synthetic E22G Aβ40 [25].

Tau filaments from case *AβPParc1* were identical to PHFs from sporadic and familial cases of AD [9, 10]. The same tau filament structures have been described in prion protein amyloidosis [13], as well as in familial British and familial Danish dementias [31]. These findings are consistent with the suggestion that the Alzheimer fold of assembled

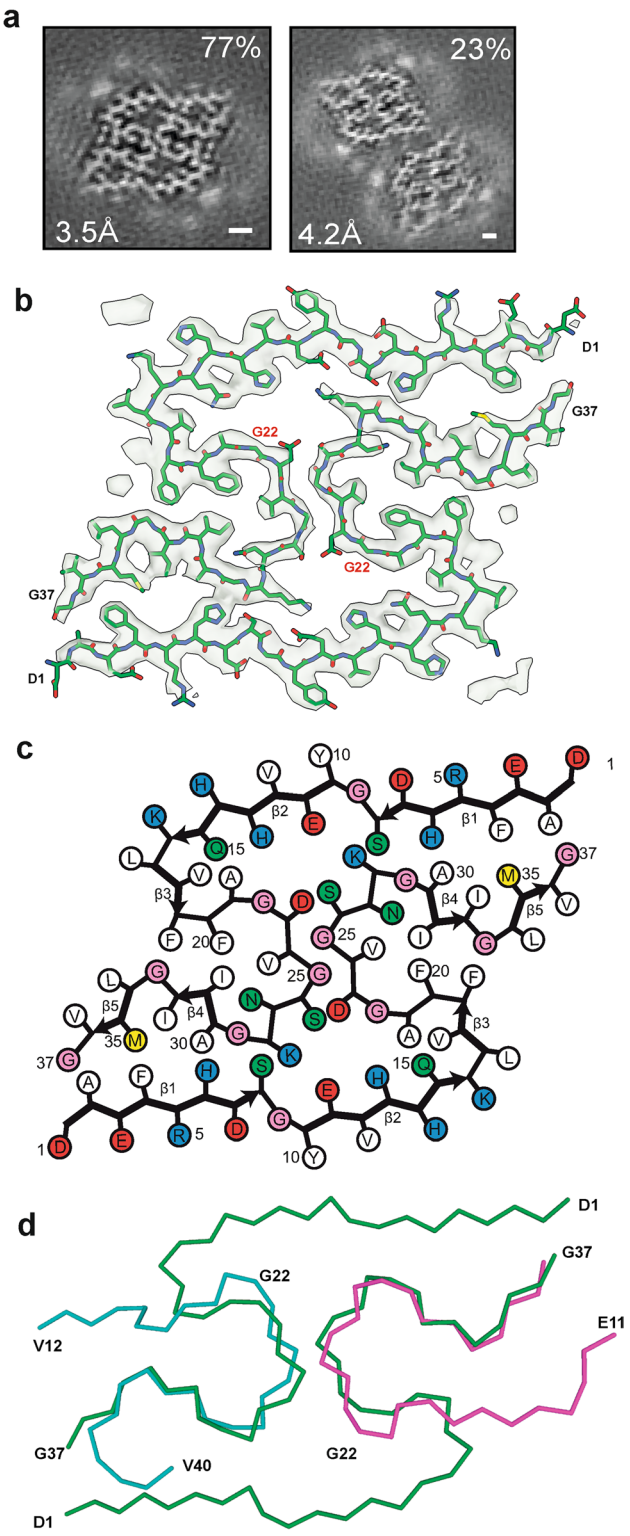

Fig. 4 The App^{NL-G-F} murine Arctic fold of Aβ. **a** Cross sections of Aβ filaments from the brains of App^{NL-G-F} mice perpendicular to the helical axis, with a projected thickness of approximately one rung. Percentages of filaments (relative to the total, taken as 100%) are shown on the top right. The resolutions of the cryo-EM maps are given on the bottom left (3.5 Å and 4.2 Å). Scale bar, 1 nm. **b** Cryo-EM density map (in transparent gray) and atomic model (in green) of App^{NL-G-F} murine Aβ filaments with the Arctic fold. **c** Schematic of App^{NL-G-F} murine Aβ filaments with the Arctic mutation. Negatively charged residues are shown in red, positively charged residues in blue, polar residues in green, non-polar residues in white, sulfur-containing residues in yellow and glycines in pink. Thick connecting lines with arrowheads indicate β-strands. **d** Superposition of the backbone structures of dimeric App^{NL-G-F} murine Arctic filament (green) and the doublet of human Arctic fold A (cyan) and human Arctic fold B (magenta). The all-atom r.m.s.d. value for pairs of common substructures (F20-G37) of human Arctic folds A and B and App^{NL-G-F} murine dimeric Arctic fold was 2.4 Å

tau is present whenever extracellular amyloid deposits form, irrespective of their structures and composition.

Experimental model systems that replicate the structures of amyloids from human brains will be crucial in furthering our mechanistic understanding of disease. We showed previously that Aβ filaments from mice of the App^{NL-F} knock-in line, which express wild-type Aβ, are identical to type II filaments from human brains [37]. Aβ filaments from the brains of mice of the App^{NL-G-F} knock-in line, which are made of two identical mutant protofilaments that extend from D1-G37, differ from both wild-type and Arctic mutation Aβ filaments from human brains. A recent study has also reported the App^{NL-G-F} murine Arctic fold using Aβ filaments extracted from the brains of 11–13-month-old homozygous App^{NL-G-F} mice [20]. By mass spectrometry, mutant Aβ42 predominated, whereas the filaments that we extracted from the brains of 22-month-old App^{NL-G-F} mice, were mostly made of mutant Aβ38, suggesting that filaments with the App^{NL-G-F} murine Arctic fold form from mutant Aβ42, with their C-terminal fuzzy coat being truncated over time.

The reasons for the differences in structure between human and App^{NL-G-F} murine Arctic folds are unknown. It has been reported that murine BACE1 only cleaves human APP at position + 1, whereas human BACE1 cleaves it at positions + 1 and + 11 [6]. It is also possible that differences in the levels of Aβ40 and Aβ42, or their relative abundance, which have been associated with the Swedish and Iberian mutations in APP, in combination with the Arctic mutation in Aβ, may affect the structures formed. Another difference is that 100% of Aβ is mutant in homozygous App^{NL-G-F} knock-in mice [28], whereas the Arctic mutation is dominantly inherited [25]. In the App^{NL-G-F} murine Arctic fold, the main chain conformation at G22 is incompatible with non-glycine residues, unlike in human Arctic folds, where other residues can be accommodated at this site with only minor conformational changes. This suggests that the incorporation of wild-type Aβ may inhibit formation and/or growth of mutant filaments with the App^{NL-G-F} murine Arctic fold, but not with the human Arctic folds.

Knock-in [28] and transgenic mouse models [8] have shown that the Arctic mutation is highly fibrillogenic when compared to wild-type Aβ. The mechanisms underlying the fibrillation-promoting effects of E22G Aβ are the same for the App^{NL-G-F} murine and human Arctic folds, namely increased hydrogen bonding between adjacent Aβ molecules and reduced electrostatic repulsion.

In summary, we report the structures of Aβ filaments from a case of AD with the Arctic mutation and from mouse knock-in line App^{NL-G-F}. These findings have implications for our understanding of AD pathophysiology. Because most filaments made of mutant Aβ differ from those formed from wild-type protein, it may be preferable to use the App^{NL-F} knock-in mouse line for studying the mechanisms underlying sporadic AD. We also provide a structural explanation for the previously observed increase in the assembly of E22G Aβ when compared to wild-type protein. However, although the E22G mutation has been reported to lead to an increase in the formation of so-called protofibrils in recombinant Aβ assemblies [25], protofibrils were not observed in Aβ assemblies extracted from human or mouse brains. Knowledge of the Aβ folds in human disease will inform the rational design of compounds that bind specifically to these filaments and the development of more relevant models for AD using in vitro assembly, cells and animals.

Supplementary Information The online version contains supplementary material available at https://doi.org/10.1007/s00401-022-02533-1.

Acknowledgements This work was supported by the Electron Microscopy Facility of the MRC Laboratory of Molecular Biology. We thank Jake Grimmett, Toby Darling and Ivan Clayson for help with high-performance computing. We acknowledge Diamond Light Source for access and support of the cryo-EM facilities at the UK's Electron Bio-imaging Centre (under proposal bi23268), funded by the Wellcome Trust, the MRC and the Biotechnology and Biological Sciences Research Council (BBSRC). M.G. is an Associate Member of the UK Dementia Research Institute.

Author contributions BG, CG, AK and AN identified the patient and performed genetic analysis and neuropathology; TS and TCS provided App^{NL-G-F} knock-in mice; JM and IL organized breeding and characterized mouse tissues; YY, MH, SL and SYP-C prepared filaments and performed mass spectrometry; YY and MS performed cryo-EM data acquisition; YY, WZ, AGM and SHWS performed cryo-EM structure determination; MG and SHWS supervised the project and all authors contributed to the writing of the manuscript.

Funding This work was supported by the UK Medical Research Council, as part of UK Research and Innovation (MC_UP_A025-1013 to S.H.W.S. and MC_U105184291 to M.G.) and by the US National Institutes of Health (UO1-NS110457).

Data availability Cryo-EM maps have been deposited in the Electron Microscopy Data Bank (EMDB) with the accession numbers EMDB 16022, 16023 and 16027. Corresponding refined atomic models have been deposited in the Protein Data Bank (PDB) under accession numbers 8BFZ, 8BG0 and 8BG9. Please address requests for materials to the corresponding authors.

Declarations

Conflict of interest The authors declare that they have no conflicts of interest.

Ethical approval Studies carried out at Indiana University and the Karolinska Institutet (2011/962-31/1) were approved through the ethical review processes at each Institution's Review Board.

Informed consent Informed consent was obtained from the patient's next of kin. This study was approved by the Cambridgeshire 2 Research Ethics Committee (09/H0308/163).

References

1. Basun H, Bogdanovic N, Ingelsson M, Almkvist O, Näslund J, Axelman K et al (2008) Clinical and neuropathological features of the Arctic *APP* gene mutation causing early-onset Alzheimer disease. Arch Neurol 65:499–505
2. Bepler T, Morin A, Rapp M, Brasch J, Shapiro L, Noble AL et al (2019) Positive unlabeled convolutional neural networks for particle picking in cryo-electron micrographs. Nature Meth 16:1153–1160
3. Bornebroek M, Haan J, Maat-Sareman MLG, van Duinen SG, Roos RAC (1996) Hereditary cerebral haemorrhage with amyloidosis-Dutch type (HCHWA-D): a review of clinical, radiologic and genetic aspects. Brain Pathol 6:111–114
4. Bucciantini M, Giannoni E, Chiti F, Baroni F, Formigli L, Zurdo J et al (2002) Inherent toxicity of aggregates implies a common mechanism for protein misfolding diseases. Nature 416:507–511
5. Bugiani O, Giaccone G, Rossi G, Mangieri M, Capobianco R, Morbin M et al (2010) Hereditary cerebral haemorrhage with amyloidosis associated with the E693K mutation of *APP*. Arch Neurol 67:987–995
6. Cai H, Wang Y, McCarthy D, Wen H, Borchelt DR, Price DL et al (2001) BACE1 is the major beta-secretase for generation of Abeta peptides by neurons. Nat Neurosci 4:233–234
7. Casañal A, Lohkamp B, Emsley P (2020) Current developments in Coot for macromolecular model building of electron cryo-microscopy and crystallographic data. Protein Sci 29:1055–1064
8. Cheng IH, Palop JJ, Esposito LA, Bien-Ly N, Yan F, Mucke L (2004) Aggressive amyloidosis in mice expressing human amyloid peptides with the Arctic mutation. Nature Med 10:1190–1192
9. Falcon B, Zhang M, Schweighauser M, Murzin AG, Vidal R, Garringer HJ et al (2018) Tau filaments from multiple cases of sporadic and inherited Alzheimer's disease adopt a common fold. Acta Neuropathol 136:699–708

10. Fitzpatrick AWP, Falcon B, He S, Murzin AG, Murshudov G, Garringer HJ et al (2017) Cryo-EM structures of tau filaments from Alzheimer's disease. Nature 547:185–190
11. Goate A, Chartier-Harlin MC, Mullan M, Brown J, Crawford F, Fidani L et al (1991) Segregation of a missense mutation in the amyloid precursor protein gene with familial Alzheimer's disease. Nature 349:704–706
12. Goedert M, Spillantini MG, Cairns NJ, Crowther RA (1992) Tau proteins of Alzheimer paired helical filaments: abnormal phosphorylation of all six brain isoforms. Neuron 8:159–168
13. Hallinan GI, Hog MR, Ghosh M, Vago FS, Fernandez A, Garringer HJ et al (2021) Structure of tau filaments in prion protein amyloidosis. Acta Neuropathol 142:227–241
14. Hardy JA, Higgins GA (1992) Alzheimer's disease: the amyloid cascade hypothesis. Science 256:184–185
15. He S, Scheres SHW (2017) Helical reconstruction in RELION. J Struct Biol 193:163–176
16. Kalimo H, Lalowski M, Bogdanovic N, Philipson O, Bird TD, Nochlin D et al (2013) The Arctic AβPP mutation leads to Alzheimer's disease pathology with highly variable topographic deposition of differentially truncated Aβ. Acta Neuropathol Commun 1:60
17. Kamino K, Orr HT, Payami H, Wijsman EM, Ela Alonso M, Pulst SM et al (1992) Linkage and mutational analysis of familial Alzheimer disease kindreds for the APP gene regulation. Am J Hum Genet 51:998–1004
18. Kollmer M, Close W, Funk L, Rasmussen J, Bsoul A, Schierhorn A et al (2019) Cryo-EM structure and polymorphism of Aβ amyloid fibrils purified from Alzheimer's disease brain tissue. Nature Commun 10:4760
19. Lambert MP, Barlow AK, Chromy BA, Edwards C, Freed R, Liosatos M et al (1998) Diffusible, nonfibrillar ligands derived from Aβ1-42 are potent central nervous system neurotoxins. Proc Natl Acad Sci USA 95:6448–6453
20. Leistner C, Wilkinson M, Burgess A, Goodbody S, Xu Y, Deuchars S et al. (2022) The in-tissue molecular architecture of β-amyloid in the mammalian brain. BioRxiv.
21. Lemoine L, Gillberg P-G, Bogdanovic N, Nennesmo I, Saint-Aubert L, Viitanen M et al (2021) Amyloid, tau, and astrocyte pathology in autosomal-dominant Alzheimer's disease variants: *AβAPParc* and *PSEN1DE9*. Mol Psychiatry 26:5609–5619
22. Levy E, Carman MD, Fernandez-Madrid IJ, Power MD, Lieberburg I, van Duinen SG et al (1990) Mutation of the Alzheimer's disease amyloid gene in hereditary cerebral haemorrhage, Dutch type. Science 248:1124–1126
23. Murakami K, Irie K, Morimoto A, Ohigashi J, Shindo M, Nagao M et al (2003) Neurotoxicity and physicochemical properties of Aβ mutant peptides from cerebral amyloid angiopathy. J Biol Chem 278:46179–46187
24. Näslund J, Schierhorn A, Hellman U, Lannfelt L, Roses AD, Tjernberg LO et al (1994) Relative abundance of Alzheimer Aβ amyloid peptide variants in Alzheimer disease and normal aging. Proc Natl Acad Sci USA 91:8378–8382
25. Nilsberth C, Westlind-Danielsson A, Eckman CB, Condron MM, Axelman K, Forsell C et al (2001) The Arctic APP mutation (E693G) causes Alzheimer's disease by enhanced Aβ protofibril formation. Nature Neurosci 4:887–893
26. Philipson O, Lord A, Lalowski M, Soliymani R, Baumann M, Thyberg J et al (2012) The Arctic *amyloid-β precursor protein (AβPP)* mutation results in distinct plaques and accumulation of N- and C-truncated Aβ. Neurobiol Aging 33:1010.e1-1010.e13
27. Rohou A, Grigorieff N (2015) CTFFIND4: Fast and accurate defocus estimation from electron micrographs. J Struct Biol 192:216–221
28. Saito Y, Matsuba N, Mihira J, Takano P, Nilsson S, Itohara N et al (2014) Single *App* knock-in mouse models of Alzheimer's disease. Nature Neurosci 17:661–663
29. Scheres SHW (2020) Amyloid structure determination in RELION-3.1. Acta Cryst D76:94–101
30. Schöll M, Wall A, Thordardottir S, Ferreira D, Bogdanovic N, Langström B et al (2012) Low PiB PET retention in presence of pathologic CSF biomarkers in Arctic APP mutation carriers. Neurology 79:229–236
31. Shi Y, Zhang W, Yang Y, Murzin AG, Falcon B, Kotecha A et al (2021) Structure-based classification of tauopathies. Nature 598:259–363
32. Stenh C, Nilsberth C, Hammarbäck C, Engwall B, Näslund J, Lannfelt L (2002) The Arctic mutation interferes with processing of the amyloid precursor protein. NeuroReport 13:1857–1860
33. Tarutani A, Arai S, Murayama S, Hisanaga SI, Hasegawa M (2018) Potent prion-like behaviors of pathogenic α-synuclein and evaluation of inactivation methods. Acta Neuropathol Commun 6:29
34. Thordardottir S, Ståhlbom AK, Almvist O, Thonberg H, Eriksdotter M, Zetterberg H et al (2017) The effects of different familial Alzheimer's disease mutations on APP processing in vivo. Alzheimer's Res Ther 9:9
35. Tomiyama T, Nagara T, Shimada H, Teroaka R, Fukushima A, Kanemitsu H (2008) A new amyloid β variant favoring oligomerization in Alzheimer's-type dementia. Ann Neurol 63:377–387
36. Walsh DM, Klyubin I, Fadeeva JV, Cullen WK, Anwyl R, Wolfe MS et al (2002) Naturally secreted oligomers of amyloid beta protein potently inhibit hippocampal long-term potentiation in vivo. Nature 416:535–539
37. Yang Y, Arseni D, Zhang W, Huang M, Lövestam S, Schweighauser M et al (2022) Cryo-EM structures of amyloid-β 42 filaments from human brains. Science 475:167–172
38. Yamashita K, Palmer CM, Burnley T, Murshudov GN (2021) Cryo-EM single-particle structure refinement and map calculation using *Servalcat*. Acta Crystallogr D 77:1282–1291
39. Zheng SQ, Palovcak E, Armache JP, Verba KA, Cheng Y, Agard DA (2017) MotionCor2: anisotropic correction of beam-induced motion for improved cryo-electron microscopy. Nature Meth 14:331–332
40. Zivanov J, Nakane T, Forsberg BO, Kimanius D, Hagen WJ, Lindahl E et al (2018) New tools for automated high-resolution cryo-EM structure determination in RELION-3. Elife 7:e42166
41. Zivanov J, Nakane T, Scheres SHW (2019) A Bayesian approach to beam-induced motion correction in cryo-EM single-particle analysis. IUCrJ 6:5–17